Journal of Astronomical Telescopes, Instruments, and Systems

AstronomicalTelescopes.SPIEDigitalLibrary.org

Initial assessment of monocrystalline silicon solar cells as large-area sensors for precise flux calibration

Sasha Brownsberger
Nicholas Mondrik
Christopher W. Stubbs

SPIE.

Sasha Brownsberger, Nicholas Mondrik, Christopher W. Stubbs, "Initial assessment of monocrystalline silicon solar cells as large-area sensors for precise flux calibration," *J. Astron. Telesc. Instrum. Syst.* **6**(2), 026001 (2020), doi: 10.1117/1.JATIS.6.2.026001

Initial assessment of monocrystalline silicon solar cells as large-area sensors for precise flux calibration

Sasha Brownsberger,[a,*] Nicholas Mondrik,[a] and Christopher W. Stubbs[a,b]
[a]Harvard University, Department of Physics, Cambridge, Massachusetts, United States
[b]Harvard University, Department of Astronomy, Cambridge, Massachusetts, United States

Abstract. As the precision frontier of large-area survey astrophysics advances toward the one millimagnitude level, flux calibration of astronomical instrumentation remains an ongoing challenge. We describe initial testing of silicon solar cells (SCs) as large-aperture precise calibration photodiodes. We present measurements of dark current, linearity, frequency response, spatial response uniformity, and noise characteristics of the Sunpower C60 SCs, an interdigitated back-contact 125×125 mm^2 monocrystalline SC. We find that these devices may hold promise as large-area flux calibration sensors and that further analyses over a broader range of operating conditions are necessary. [DOI: 10.1117/1.JATIS.6.2.026001]

Keywords: instrumentation; detectors techniques; photometric methods; laboratory; solid state.

Paper 19106 received Sep. 30, 2019; accepted for publication Mar. 16, 2020; published online Apr. 2, 2020.

1 Introduction

Flux calibration remains a primary source of systematic uncertainty in the use of type Ia supernovae (SNe Ia) as probes of the history of cosmic expansion.[1–4] The wavelength-dependent throughput of the observing instrument is the most immediately accessible and separable contribution to this systematic error. One approach for flux calibration is to invoke models of photon emission spectra versus wavelength for a simple stellar atmosphere, white dwarf stars being the most popular.[5] This calibration method includes contributions from the instrument throughput but is also affected by uncertainties in galactic and atmospheric extinction and other systematic effects. A supplemental approach that isolates the instrument throughput is to use well-characterized sensors as the metrology standard for relative flux determination.[6–10] In this approach, a well-calibrated photodetector, known to better than a part per thousand,[11] is used to map out the instrument's relative sensitivity versus wavelength. Conventional photon-detectors [photodiodes (PDs), CCDs, etc.] have collection areas no larger than a few square centimeters. Such small collection areas are inadequate for some modern imaging applications that depend on the calibration of a large-diameter optical beam.

The Large Synoptic Survey Telescope[12] (LSST) project intends to use a collimated, monochromatic beam (a collimated beam projector or CBP) to sequentially illuminate portions of the optics, and a calibrated silicon PD to monitor the flux.[13,14] The LSST team plans to use the CBP to measure instrument transmission as a function of photon wavelength and source position.

One metrology challenge of this approach is to measure the flux emanating from the CBP, which has an exit pupil diameter of 240 mm, about 20 times larger than the diameter of typical silicon PDs. The LSST team is considering several solutions to this unsolved problem, including changing the projector beam focus to reduce the spot size, collecting the light with a focusing concentrator, using an integrating sphere (IS) with a 250-mm port, or scanning the exit beam across one or more standard calibrated PDs. Each of these approaches, all suboptimal, are born of a perceived need to measure a large light source with a small detector.

There is nothing fundamental to the process of flux calibration that mandates the use of a sensor with a small collecting area. Indeed, photon-to-electron converters with large collection areas are already in use in the form of photovoltaic cells. Using a large-area calibration sensor

*Address all correspondence to Sasha Brownsberger, E-mail: sashabrownsberger@g.harvard.edu

allows for increased photon detection rates without the need for intervening focusing optics that themselves require calibration. In addition, modulation of the calibration light can be used to discriminate between background and calibration illumination. In this paper, we consider the possibility of using an array of high-efficiency solar cells (SCs) as a full-aperture sensor for calibrating the LSST CBP and other large-diameter internal calibration light sources.

In Sec. 2, we describe the general architecture of an interdigitated back-contact monocrystalline silicon SC and introduce the C60 SCs that we study. In Sec. 3, we describe the methods and results of our measurements. We conclude in Sec. 4, where we summarize the results of our experiments and discuss additional steps that should be taken to fully assess the prospect of creating a precision photometric calibrator composed of SCs.

2 Back-Contact Silicon Solar Cells

As with astronomical CCDs and other silicon photosensors, SCs exploit the bandgap in silicon to convert incident photons into electron–hole pairs. The challenge is to extract these charge carriers from the bulk material.

We seek a two-terminal device that sweeps charge carriers out of the bulk and into an external circuit, where photocurrent is used to determine incident flux. A standard approach is to apply a bias voltage along the photon incidence direction to produce an axial electric field that sweeps the charge out of the device. This requires electrical contact to the surface that the light strikes, which can compromise efficiency due to reduced fill factor or increased reflection. Back-contact SCs,[15–17] on the other hand, have both the anode and cathode on the nonilluminated (back) side of the silicon slab. Doping on the front side serves to repel charge carriers and drive them to the anode (or emitter) where they are collected. Implants aligned with back-side electrodes produce a series of PN junctions.

2.1 *Conceptual Design of Back-Contact Solar Cells*

We present a conceptual illustration of the back-contact SC layout in Fig. 1.

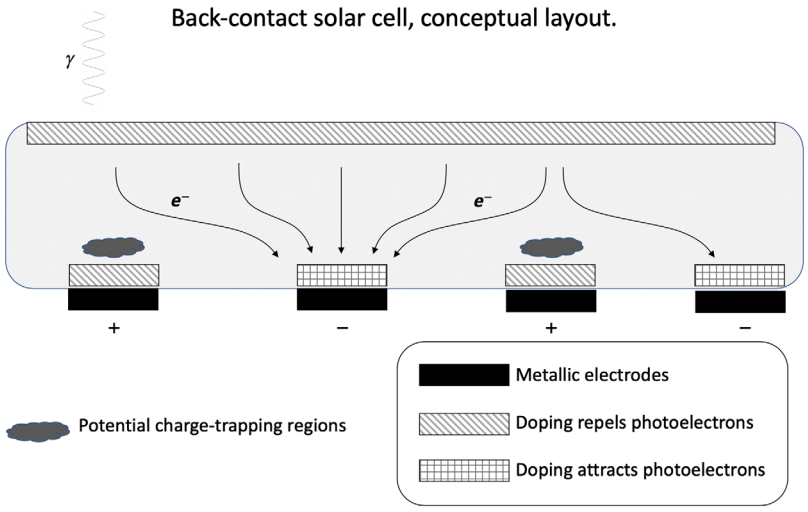

Fig. 1 Simplified illustration of an interdigitated back-contact SC architecture.[17] The polarity labels match those on the C60 SCs and indicate the direction of current flow when an external load is attached. Light incident from the top in this diagram creates electron–hole pairs in the monocrystalline silicon, and the resulting photocharge moves to back-side electrodes that reside under doped regions. The PN junction occurs between the electrodes and creates lateral electrical fields. A layer of doping on the top surface drives the electrons away from surface states and creates a local vertical electric field component. As we discuss in Sec. 3.5, the periodicity of the electrode/doping structure may give rise to regions where charge trapping can occur, degrading the effective quantum efficiency (EQE).

The device's quantum efficiency (QE), the number of collected charge carriers per incident photon, is a function of incident photon wavelength, λ. As with CCDs, the index of refraction mismatch produces reflections, especially for $\lambda < 400$ nm. At long wavelengths, the limitation is photon energy approaching the bandgap.

In our use of SCs as photometric calibrators, we care about their efficiency in turning incident photons into measurable electrical current, what we refer to as their EQE. This stands in contrast to the conventional application of SCs in generating renewable energy, where the figure of merit is the fraction of incident solar energy converted into useful electrical power or the energy efficiency. A single incident photon excites a single electron, but all energy of the incident photon in excess of the bandgap energy is lost as heat. Thus, a cell's EQE is generally greater than its energy efficiency.

Note that a cell's EQE is the product of its true QE and the fraction of the excited electrons that are successfully driven across the current-amplifier load. It is always true that QE > EQE.

In back-contact SCs, the electrical potential is periodic in the direction perpendicular to the electrodes, creating a series of regions where the perpendicular electric field is zero. This will reduce the QE of the device if the charge carriers dwell in these regions of null electric field long enough to recombine, or if these corrugations in the electrical potential trap photon-excited charges. We search for and discuss the spatial dependence of a cell's EQE in Sec. 3.5.

Other internal loss mechanisms can also reduce the SC QE. These mechanisms include charge traps (local minima in the electrical potential energy), undesirable energy levels from contamination and defects, and electron–hole recombination. Manufacturers have worked hard to maximize the QE of silicon SCs by minimizing these effects and by applying an antireflection (AR) coating to the detecting surface to minimize reflections. The QE of contemporary SCs is in excess of 95% over much of the wavelength range of interest.[18,19] Detailed simulations of the charge collection efficiency as a function of electrode geometry and doping concentration[20] have been useful in guiding the design of these devices.

2.2 *Useful Equivalent Circuit*

In analyzing the properties of a SC, we found it useful to model the cell's electrical behavior using a simple equivalent circuit (EC). In this work, we use the standard single-diode EC[21] shown in Fig. 2. A more robust analysis could generalize to a two-diode model[22,23] to account for distinct recombination timescales.

In this model circuit, a pair of current sources drive current toward the output terminals. One source, I_L, increases monotonically with the incident light. The other, I_B, sources the bias current. With no external load, these currents flow through the system's internal diode, shunt

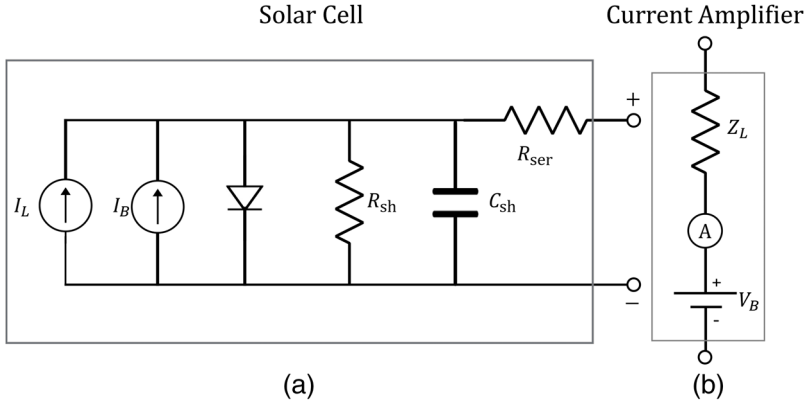

Fig. 2 (a) The single-diode EC and (b) current-source EC for the current amplifier that we use to characterize the C60 SCs. Our measurements suggest that every C60 SC has distinct characteristic values. Typically, $R_{ser} \sim \mathcal{O}(0.01 \text{ to } 0.1\ \Omega)$, $R_{sh}^{1\ \mu A} \sim \mathcal{O}(100 \text{ to } 1000\ \Omega)$, and $C_{sh} \sim \mathcal{O}(1 \text{ to } 10\ \mu F)$. The arrows of the current sources indicate the direction of current flow relative to the polarity designations (±) on the electrodes of the C60 SC.

resistance, R_{sh}, and shunt capacitance, C_{sh}. When the SC is connected to an electrical load, such as a current amplifier, current is also driven across this load in series with the cell's series resistance, R_{ser}. Our tests in Secs. 3.2 and 3.4 find that this single diode circuit is a good model for the C60 SCs with one notable exception: when back biased, the cell's current response deviates from the linear behavior expected from R_{sh}, presumably due to quantum tunneling.[24]

2.3 *Specific Example: C60 Solar Cells*

We obtained a sample of Sunpower C60 monocrystalline back-contact silicon SCs ("C60 SCs" henceforth) from the Amazon online storefront.

The C60 SCs are 125-mm truncated square silicon elements with interdigitated anode and cathode electrodes. The front (illuminated) side has no electrical connection and the electrodes on the back (dark) side have solder tab connections. The vendor advertises an AR coating as having been applied to enhance photon conversion efficiency in the blue. The vendor claims a QE of >0.95 for λ between 500 and 900 nm and a QE of >0.9 for λ between 400 and 1050 nm, consistent with the modern standards for interdigitated back-contact SCs.[18,19]

The vendor's specifications are listed in Table 1. Front and back images of a C60 SC are shown in Fig. 3.

Table 1 Manufacturer's characteristics of C60 SC.

Property	Value
Material	Monocrystalline silicon
Side length	125 mm
Thickness	165 μm
Short-circuit current in 1000 W/m^2 illumination	6.3 A
Open circuit voltage in 1000 W/m^2 illumination	0.68 V
Max-power output voltage in 1000 W/m^2 illumination	0.58 V
Max-power output current in 1000 W/m^2 illumination	5.9 A

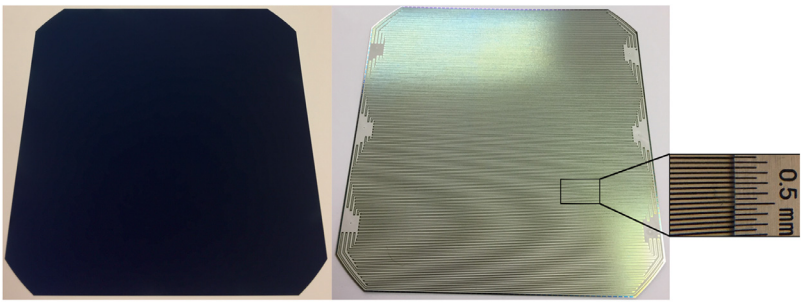

Fig. 3 (a) Front and (b) back images of a C60 SC. The cells are 125 mm squares with truncated corners. The magnification of the back side shows the electrodes (silver bands) fused to the back of the silicon surface (dark bands) with a ruler for scale. Parallel electrodes sit alternately at positive and negative voltages. Parallel electrodes are 0.46 mm apart and parallel electrodes of matching electric potential are 0.92 mm apart.

3 Preliminary Characterization of C60 Solar Cells

3.1 *Preparing the Cells for Use*

The C60 SCs do not come with any external wires for connection to other devices. The manufacturer recommends that the user directly solder a pair of specially designed "interconnect" tabs, one for the anode and one for the cathode, to the system's solder points. However, we found that soldering the SCs directly caused their unbiased dark currents to increase by a factor of 5 to 100 or more. Any nonphotoelectric current introduces measurement error (both statistical and systematic) and ought to be minimized.

We soldered wire leads to the interconnect tabs and used electrically conductive copper tape, reinforced with nonconductive super glue, to affix the interconnect tabs to the SCs. This method produced stable connections at room temperature without degrading the dark current. However, we are concerned about these attachment's multiyear reliability and their stability under large current loads. We suspect that a conducting adhesive would yield better long-term results.

3.2 *Unilluminated IV Curve of C60 Solar Cell*

As we model in Fig. 2, a current amplifier attached to the output SC imposes a bias voltage, V_b, and carries a load impedance, Z_L. An ideal current amplifier has both $V_b = 0$ and $Z_L = 0$. When a current, I_{Out}, passes through the load, the voltage drop over the series resistance and the load will drive a current, I_{sh}, through the shunt impedance, Z_{sh}:

$$I_{\mathrm{sh}} Z_{\mathrm{sh}} = V_b + I_{\mathrm{Out}}(R_{\mathrm{ser}} + Z_L). \tag{1}$$

Current generated within the SC, I_{SC}, will split between the shunt impedance and the load:

$$I_{\mathrm{SC}} = I_{\mathrm{Out}} + I_{\mathrm{sh}}. \tag{2}$$

The fraction of the SC current that passes through the load is thus dependent on the applied bias voltage and the ratio of the impedances:

$$\frac{I_{\mathrm{Out}}}{I_{\mathrm{SC}}} = \frac{r}{1+r} - \frac{V_b}{(R_{\mathrm{ser}} + Z_L + Z_{\mathrm{sh}}) I_{\mathrm{SC}}}, \tag{3}$$

where $r \equiv Z_{\mathrm{sh}}/(R_{\mathrm{ser}} + Z_L)$ defines a figure of merit for the SC and load. For light sources modulated at frequencies <100 Hz, $Z_{\mathrm{sh}} \simeq R_{\mathrm{sh}}$.

A value of $I_{\mathrm{Out}}/I_{\mathrm{SC}}$ less than unity reduces the EQE of the detector over all photon wavelengths. Any variations in the resistances or in the bias voltage will produce a wavelength-independent, systematic change in the cell's EQE and a corresponding error in flux measurements. Furthermore, because the shunt impedance of the SC is nonohmic [see Fig. 4(b)], this QE reduction depends on the incident light intensity and is a potential source of system nonlinearity. It is paramount that r be kept as large as possible by minimizing the series resistance and by maximizing the shunt resistance. In practice, this means making good electrical connections and selecting SCs with the largest values of R_{sh}.

To better understand the device-to-device variation in r, we measured the shunt and series resistances of 37 C60 SCs before affixing the conducting tabs.

According to the EC of Sec. 2.2, I_{Out} for an unilluminated SC with forward-bias voltage, V_{fb}, is determined by Ohm's law:

$$I_{\mathrm{Out}} = V_{\mathrm{fb}}/R_{\mathrm{sh}}, \tag{4}$$

where we ignore the cell's bias current, assume $R_{\mathrm{sh}} \gg R_{\mathrm{ser}}$, and assume that V_{fb} is less than the conducting voltage of the diode. Using Eq. (4), we measured the shunt resistance of each cell by fitting a line to the IV curve acquired by applying dc bias voltages ranging from -100 to 100 mV in 10 mV increments to the output terminals of unilluminated SCs.

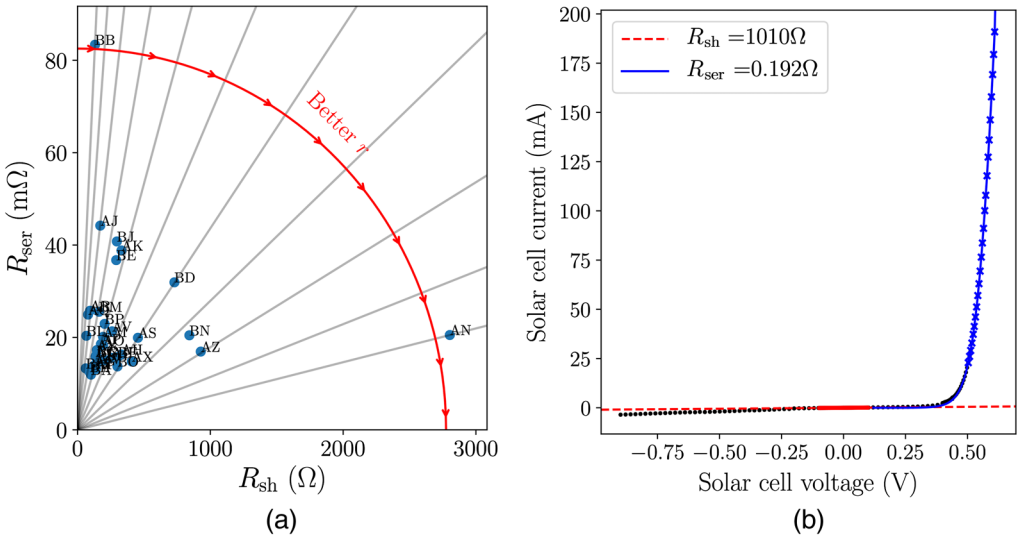

Fig. 4 The measured shunt and series resistances (R_{sh} and R_{ser}) of 37 unmodified C60 SCs (a) and the full unilluminated *IV* curve of the AX SC after wiring (b). In (a), each point is a different SC with a sequentially assigned label and the line with arrows shows increasing values of the figure of merit, $r = R_{sh}/(R_{ser} + R_L)$ when the load resistance, R_L, is negligible. Those cells with the largest value of r, in this case cells AN, AZ, and BN, are the best candidates for use in a precision photometric calibrator. In the right plot, we measured the *IV* curve of the AX SC. We fit those points for applied voltages above 500 mV (crosses) to measure a best fit value of $R_{ser} = 0.192\ \Omega$ (blue solid line) and we fit those points with applied voltages between ± 100 mV (red dots) to determine a best fit value of $R_{sh} = 1010\ \Omega$ (red dashed line). Comparing these results to the measured resistances before the cell was wired [the point labeled "AX" in (a)], the shunt resistance is about 120% larger and the series resistance is about 1300% larger. The increased series resistance is likely due to the resistance of the affixed wiring and underscores the importance of good electrical contacts and short electrical leads. The increase in shunt resistance is somewhat surprising and something that we do not presently understand.

When the applied voltage biases the diode into conduction, R_{sh} is shorted and has a negligible effect on the cell's internal resistance. The dc behavior of the cell in this regime is determined entirely by the summed impedances of the diode and the series resistance:

$$V_{fb} = V_{di} + V_{Rser} = \ln(I_{Out}/I_s) n k_B T + I_{Out} R_{ser}, \tag{5}$$

where k_B is Boltzmann's constant, T is the temperature of the silicon, n is the diode quality factor (typically between 1 and 2),[25] and I_s is the diode saturation current. We measured R_{ser} for 37 SCs by fitting Eq. (5) to the portion of the unilluminated *IV* curve for which $V_{fb} \geq 0.5$ V. We let R_{ser}, nk_BT, and I_s vary freely in the fit.

In Fig. 4(a), we show the measured values of R_{sh} and R_{ser}, along with contours for the r figure of merit assuming a shorted load.

Opting to preserve those cells with the largest values of r for future projects, we measured the full, unilluminated room-temperature *IV* curve of the C60 SC "AX" after affixing electrical leads by the process described in Sec. 3.1. We show this curve in Fig. 4(b). To measure the ohmic behavior of the cell for small dc bias voltages, we fit a line to those points for which the magnitude of the applied voltage is below 100 mV [red points in Fig. 4(b)] and took the inverse of the fitted slope as the shunt resistance, R_{sh}. To measure the cell's series resistance, R_{ser}, we fit the *IV* curve for points with forward-bias voltages above 0.5 V [blue points in Fig. 4(b)] using Eq. (5). These two slopes imply a R_{sh} and R_{ser} of 1010 and 0.192 Ω, respectively. By fitting the current of the cell for applied voltages <3 mV in magnitude, we measured the cell's intrinsic dark current, I_B, to be 2 nA.

Although these cells partially conform to the behavior predicted by the EC of Fig. 2, they are nonohmic. For example, cell AX has a nonlinear reverse current response to increasing back-bias voltages [negative voltages in Fig. 4(b)]. A back-bias voltage of 400 mV drives 3.4 times more

reverse current through the SC than the EC predicts, with the disparity growing more extreme as the back-bias voltage grows.

3.2.1 *Hypothetical method for canceling dc currents*

We anticipate using these devices in a mode where the light source of interest is modulated in order to distinguish calibration light from background illumination. The symmetrical ohmic behavior of these devices near zero applied bias voltage opens up the interesting possibility of applying an actively controlled bias voltage in order to drive a leakage current that cancels the sum of dark current and dc photocurrent from background illumination. This will reduce the Poisson noise at the modulation frequency even if the cancelation is imperfect. Noise arising from fluctuations in the background level at the modulation frequency will remain a limitation.

If the calibration light is modulated with a square wave, a fast A/D converter could monitor the net dc current when the light is in the off state and could change the applied bias to minimize this value. An analog circuit could be designed to accomplish the same task.

3.3 *Determining Nonlinearity of QE*

We define the nonlinearity of a SC as the dependence of its QE on the incident photon flux, ϕ. An ideal SC is perfectly linear, meaning its QE is entirely independent of ϕ. Our method for determining the nonlinearity of the C60 SCs combines the simultaneous illumination of a reference and uncharacterized detector[26] with the use of a lock-in (LI) amplifier.[27]

We used a Stanford Research Systems (SRS) DS345 function generator to drive a set of Thorlabs LEDs, listed in Table 2, with a 13 Hz 0 to 2 V square wave. We connected the LEDs to a 1.5-mm-diameter optical fiber, which illuminated one port of a Thorlabs 2" IS through a logarithmically varying neutral density (ND) filter and an iris. A Thorlabs SM1PD2A PD occupied another IS port, and the SC stood several inches away from a third IS port. The IS ports for the fiber, the PD, and the SC were mutually orthogonal. The SC's collecting area was overfilled by the output of the IS. BNC cables connected both the SC and the PD to a BNC switch box, the output of which we connected to an SRS SR570 current preamplifier. We fed the output of the preamplifier into the input of an SRS SR2124 LI that was synchronized to the frequency of the function generator. The BNC switch box toggled between the PD and SC signals, both subject to the same loading effects of the downstream instruments. By moving the position of the variable ND filter with a translation stage, we changed the illumination intensity of the IS.

In Fig. 5, we measure the cell's linearity by plotting the normalized ratio of the SC- and PD-modulated currents as a function of SC current densities assuming homogeneous illumination. This ratio is constant to within 1% over the range of monitored fluxes, suggesting that the C60 SCs are linear to within 1% for photocurrent densities between $\sim$100 pA/cm^2 and $\sim$100 nA/cm^2 for the wavelengths tested. The LSST CBP remains in development.[14] Internal estimates predict current densities of $\mathcal{O}(10\,\text{to}\,100\ \text{pA/cm}^2)$ for a monochromatic beam with adjustable wavelengths between 300 and 1100 nm. The linearity tests reported here demonstrate

Table 2 The Thorlabs LEDs[a] used to study the linearity of the C60 SCs.

LED ID[a]	Nominal wavelength (nm)	Nominal power through 1500 μm diameter fiber (mW)[b]
M365FP1	365	300.0
M415F3	415	390.0
MINTF4	554	480.0
M625F2	625	320.0

[a]More information available in Ref. 30.
[b]Inferred from reported power through a 200-μm fiber assuming optical power scales with cross-section area.

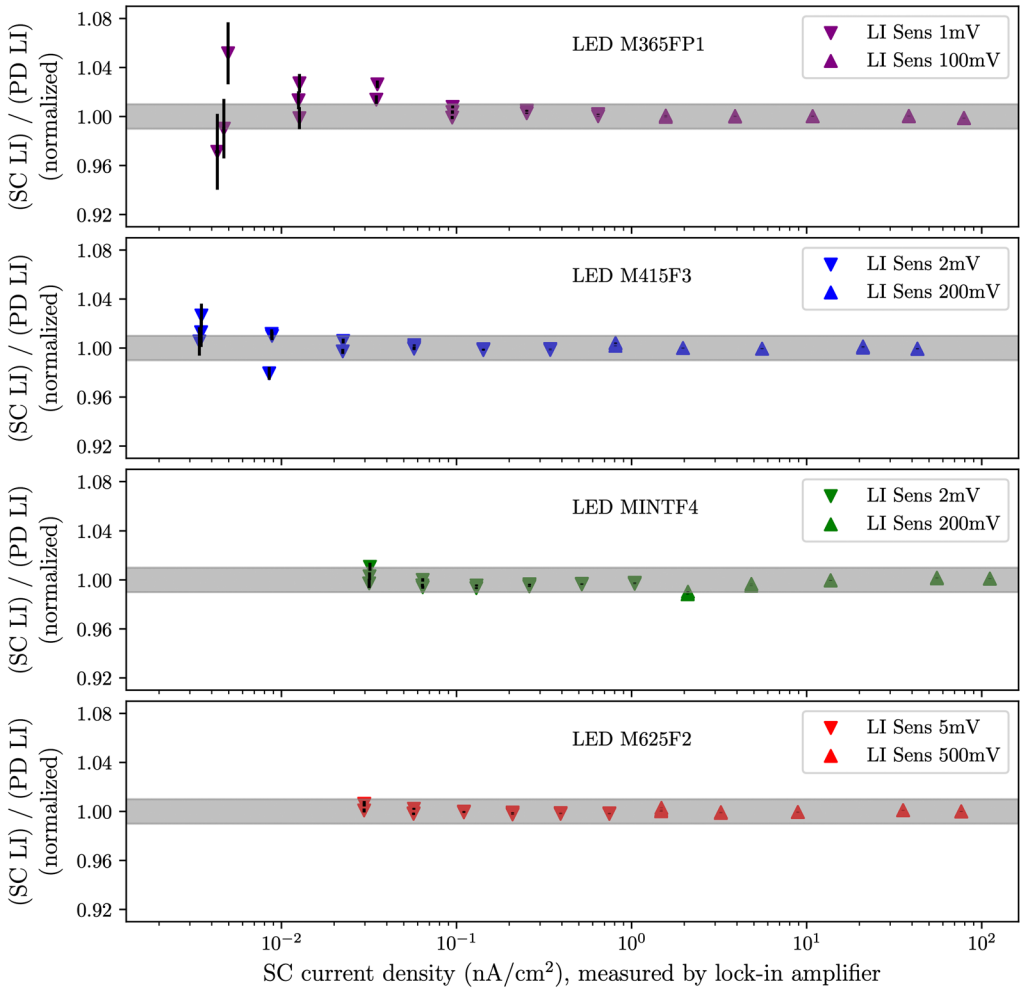

Fig. 5 C60 SC nonlinearity measured using an LI amplifier for the LEDs listed in Table 2 measured relative to a Thorlabs SM1PD2A PD. On the *x* axis, we plot SC current density assuming that the photocurrent is generated uniformly across the cell surface. On the *y* axis, we plot the ratio of SC and photodiode currents, both measured using the same LI amplifier. The ratios have been normalized to unity, and the gray shadings show the $\pm 1\%$ linearity bounds. Based on these results, the SC is linear to within 1% for photocurrent densities between $\sim$100 pA/cm^2 and $\sim$100 nA/cm^2 for incident photon wavelengths between 365 and 625 nm.

1% linearity over a portion of this expected CBP parameter space, but further verification may be necessary when the design is finalized.

3.4 *Rise Time/Frequency Response*

We are interested in applications where the calibration light is modulated at some modest frequency to discriminate calibration light from ambient light. To determine a SC's viability as a calibrator for such a modulated light source, we must determine two semidistinct frequency dependencies.

1. As the modulation frequency increases, more photocurrent will be discharged over the SC's shunt capacitance.
2. If the EQE of the detector diminishes as the modulation frequency of the light source increases, possibly due to non-negligible collection and diffusion times of the charge carriers,[28,29] the produced photocurrent will diminish and the output signal will drop.

Both of these effects could reduce the amplifier signal as the frequency of modulation increases.

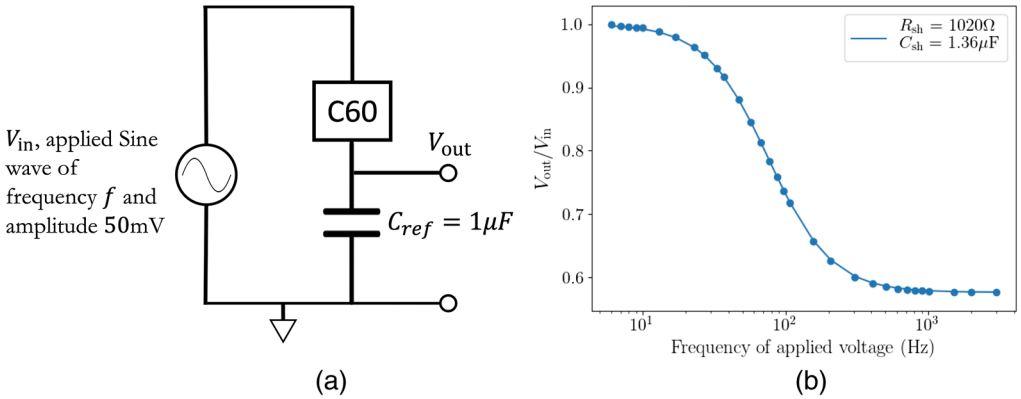

Fig. 6 (a) Circuit configuration for measuring frequency dependence of C60's parallel impedance and (b) the results of that measurement. We fit the measured voltage ratio values (points) to the voltage ratio predicted in Eq. (6) with the extracted best-fit values of $R_{sh} = 1020\ \Omega$ and $C_{sh} = 1.36\ \mu$F (line). The ~1% disparity between this measurement of R_{sh} and the measurement of R_{sh} derived from the unilluminated *IV* curve (Fig. 4) is likely due to the cell's non-ohmic *IV* response.

We measured the shunt impedance of the SC, $Z_{SC}(f)$, by measuring the voltage across a series capacitance of 1 μF given an applied 50-mV peak-to-peak sinusoidal voltage of varying frequency. The output voltage, V_{Out}, is determined by $Z_{SC}(f)$ and by the impedance of the reference capacitor, $Z_{ref}(f) = -i(2\pi f C_{ref})^{-1}$, according to

$$\frac{V_{Out}(f)}{V_{in}(f)} = \frac{Z_{ref}(f)}{Z_{ref}(f) + Z_{SC}(f)} = \frac{1}{1 + 2\pi i f C_{ref} Z_{SC}(f)}. \tag{6}$$

In Fig. 6, we show both this measurement scheme and the results of applying this measurement to SC "AX." We found that the EC model of Fig. 2 effectively describes the shunt impedance of the SC up to an input frequency of at least 3 kHz for voltages $\lesssim$50 mV.

We repurposed the configuration used to measure the SC linearity (Sec. 3.3) to measure the SC's response to modulated light. Our results are dominated by the gain bandwidth product of the current amplifier and by the upper frequency limit of the LED driver. We determined that the SC has an acceptable time response out to at least 200 Hz.

3.5 *Spatial Uniformity of QE*

The electrodes along the back of the C60 SCs (see Fig. 3) produce a corrugated electric potential that may adversely affect the QE. To determine the strength of this effect, if it exists at all, we illuminated a 30-μm pinhole with the M415F3 Thorlabs LED (see Table 2). We used a pair of convex lenses to image the pinhole onto the surface of SC "AX," forming a 150-μm diameter spot. We used a translation stage to scan the pinhole image across the cell parallel to the electrodes, perpendicular to the electrodes, and diagonally with respect to the electrodes. We show the results of these three scans in Fig. 7.

The response of the SC as the 150 μm spot is moved parallel to the electrodes is characterized by a series of sharp "troughs" of varying depths. Fourier analysis indicates that the spacing between these troughs is 1.2 mm, ~2.5 times larger than the spacing between adjacent electrodes of opposite polarity. It is unclear if this spatial variation is caused by the corrugations in the electric field produced by the electrodes or due to some other regularly structured spatial inhomogeneity in the SC.

In the parallel and diagonal scans, the spot obliquely traversed the electrodes and produced a series of much broader troughs in the measured current. These broader troughs contain considerable substructure, suggesting that the QE response along the electrodes is not homogeneous.

This spatial dependence of the cell's QE introduces a source of systematic error that will diminish as the cross section of the incident light grows. To assess the effect of this systematic

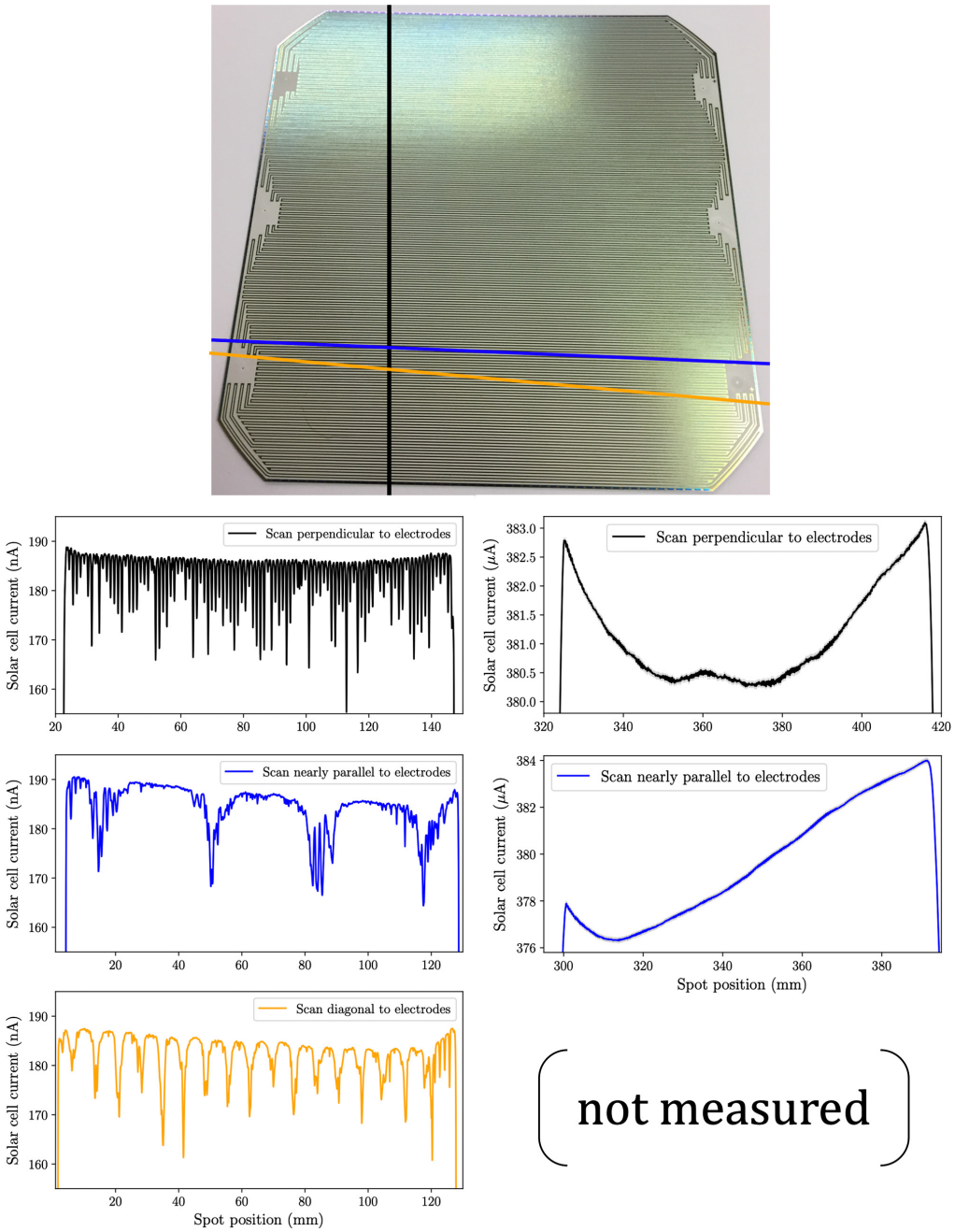

Fig. 7 C60 spatial response to scans of a 150-μm-diameter spot (lower-left column) and to scans of a 30-mm-diameter spot (lower right column) across the front of the cell as the spot is moved perpendicular to the electrodes (black), nearly parallel to the electrodes (blue), and offset 10 deg from parallel to the electrodes (orange). We show the approximate orientation of the scans with respect to the electrodes in the included image of the back side of the cell. For the small spot moving perpendicular to the electrodes, the SC signal is characterized by a series of sharp "troughs" in which the response drops by between 1% and 17%. These troughs are 1.2 mm apart. The considerable structure within the troughs of the small spot's diagonal and parallel scans indicates that the SC response is highly nonuniform along the troughs. Some $\lesssim$0.04% variations at the $\mathcal{O}$(1 mm) spatial scale are apparent in the SC response to both the the perpendicular and parallel scans of the 30-mm spot.

error on large optical beams, we scanned a 30-mm-diameter spot across the cell parallel and perpendicular to the electrodes. The results of these scans are shown in Fig. 7. Spatial variations in induced current on the scale of the electrode width are visible in both the perpendicular and parallel scan but are no bigger than 0.04%. These scans also exhibit a $\mathcal{O}$ (10 to 100 mm)

large-scale spatial inhomogeneity in the cell's QE that is as large as 4%. When using these devices as precision calibration tools, the location of the incident beam should be kept stable to minimize the systematic error introduced by such large-scale spatial inhomogeneities.

3.6 *Statistical Uncertainty*

We are primarily concerned with the statistical uncertainty due to Johnson noise[31] in the resistances and due to shot noise in the photocurrent, I_L. If we assume that the photocurrent is substantially larger than both the bias current and the current driven over the shunt resistance due to the load's bias voltage, we can estimate the statistical uncertainty in the load current, $\sigma_{I,\mathrm{Out}}$, by adding the shot noise and the Johnson noise in quadrature:

$$\mathrm{SNR} = \frac{\langle I_{\mathrm{Out}} \rangle}{\sigma_{I,\mathrm{Out}}} = \frac{\langle I_L \rangle}{\sqrt{2\langle I_L \rangle e \Delta f + 4 k_B T \Delta f (1 + 1/r) R_{\mathrm{sh}}^{-1}}}, \tag{7}$$

where $\langle \cdot \rangle$ denotes the expectation value, e is the electron charge, Δf is the monitored bandwidth, k_B is the Boltzmann's constant, T is the temperature of the SC, R_{sh} is the shunt resistance, and r is the resistor ratio figure of merit defined in Sec. 3.2. For a SC with $r \gg 1$ and $R_{\mathrm{sh}} = 500\ \Omega$ operating at $T = 300$ K, the expected contributions from shot noise and Johnson noise are equal when $I_L \simeq 100\ \mu$A. Poisson-noise-limited performance requires $I_L > 100\ \mu$A.

4 Conclusions and Next Steps

We have measured the electrical properties, linearity, frequency response, spatial uniformity, and noise characteristics of C60 back-contact monocrystalline SCs. We undertook this exploration in the hopes that these cells might serve as precise photometric calibrators for the LSST's CBP and for other large area light sources. Our results are promising, though they are only preliminary.

In Sec. 3.2, we measured the electrical properties of unilluminated SCs assuming the EC model of Fig. 2. We found that typical cells have shunt resistances $\mathcal{O}(100$ to $1000\ \Omega)$ and series resistances $\mathcal{O}(0.01$ to $0.1\ \Omega)$. The modest shunt resistances mean that even 0.1 mV of applied bias voltage can produce $\mathcal{O}(0.1$ to $1\ \mu\mathrm{A})$ of dark current. When using these SCs as precision calibrators, steps should be taken to minimize inadvertently applied bias voltages by, e.g., nonideal current amplifiers. We also measured an extensive IV curve for a single SC and found a nonlinear current response to back bias voltages, presumably due to quantum tunneling.

In Sec. 3.3, we used an LI amplifier and a set of LEDs to measure the dependence of a cell's QE on the total incident flux (its "linearity"). The cell showed <1% variation in QE for photocurrent densities between 100 pA cm^{-2} and 100 nA cm^{-2}.

In Sec. 3.4, we determined that the cell's frequency response to a modulated light source is nearly unity for modulation frequencies <200 Hz. Additional study is needed before they can be used for higher modulation frequencies.

In Sec. 3.5, we found that the SC QE varied by as much as 17% as we moved a 150-μm-diameter spot perpendicular to the cell's electrodes. We suspect that this QE variation results from corrugations in the cell's electrical potential, though the apparent mismatch between the electrode spacing (0.46 mm) and the spacing of the QE troughs (1.2 mm) is something that we do not yet understand. This spatial variation in QE constitutes a source of systematic error that will diminish as the cross section of the incident beam grows. For a beam of diameter $\geq$30 mm, the systematic error in QE resulting from this effect is $\leq$0.04%.

In Sec. 3.6, we discussed some sources of statistical error. The statistical fluctuations in our measurements will be dominated by shot noise for photocurrents $\gtrsim 100\ \mu$A.

As we described in Sec. 3.2, the flow of current over the resistance of attached electrical leads will drive a smaller current through a cell's modest shunt resistance. Variation with time or temperature in these resistances will produce a commensurate time dependence in the cell's EQE, introducing a systematic error. We believe this effect constitutes the largest obstacle to employing these cells as subpercent photometric calibrators. We are also optimistic that this obstacle can

be surmounted by minimizing the resistance of the leads and of the connections to the current amplifier, by selecting those cells with the largest shunt resistances, and by carefully controlling systematic voltage and resistance drifts.

Our results and the QE of modern interdigitated back-contact SCs[18,19] suggest that back-contact monochrystalline SCs may serve as precision photometric calibrators for large beams. However, further analyses are necessary. Some of the problems most salient to realizing this goal are: (1) improving the electrical connections of the cells, (2) measuring the cell linearity at 0.1% precision over the LSST CBP parameter space, analyzing the (3) temperature dependence and (4) long-term stability of the cell's electrical properties, (5) measuring the cell's responsivity at higher modulation frequencies, and (6) concretely determining the physical source of the spatial variation of the cell's QE. We intend to continue studying the properties of these and other SCs, and we encourage other researchers to do the same.

Acknowledgments

We thank the US Department of Energy and the Gordon and Betty Moore Foundation for their support of our LSST precision calibration efforts, under DOE Grant No. DE-SC0007881 and award GBMF7432, respectively. This material is also based partially upon work supported by the National Science Foundation Graduate Research Fellowship Program under Grant No. DGE1745303. Any opinions, findings, and conclusions or recommendations expressed in this material are those of the authors and do not necessarily reflect the views of the National Science Foundation.

References

1. R. C. Bohlin, K. D. Gordon, and P.-E. Tremblay, "Techniques and review of absolute flux calibration from the ultraviolet to the mid-infrared," *Publ. Astron. Soc. Pac.* **126**(942), 711–732 (2014).
2. C. W. Stubbs and Y. J. Brown, "Precise astronomical flux calibration and its impact on studying the nature of the dark energy," *Mod. Phys. Lett. A* **30**(40), 1530030 (2015).
3. D. Scolnic, "Relative photometric calibration of optical surveys," *J. Instrum.* **12**(04), C04021 (2017).
4. D. Scolnic et al., "The next generation of cosmological measurements with type Ia supernovae," arXiv:1903.05128 (2019).
5. G. Narayan et al., "Subpercent photometry: Faint da white dwarf spectrophotometric standards for astrophysical observatories," *Astrophys. J. Suppl. Ser.* **241**(2), 20 (2019).
6. C. W. Stubbs and J. L. Tonry, "Toward 1% photometry: end-to-end calibration of astronomical telescopes and detectors," *Astrophys. J.* **646**(2), 1436–1444 (2006).
7. G. Bernstein et al., "Instrumental response model and detrending for the dark energy camera," *Publ. Astron. Soc. Pac.* **129**(981), 114502 (2017).
8. S. Lombardo et al., "SCALA: in situ calibration for integral field spectrographs," *Astron. Astrophys.* **607**, A113 (2017).
9. C. W. Stubbs et al., "Precise throughput determination of the PanSTARRS telescope and the gigapixel imager using a calibrated silicon photodiode and a tunable laser: initial results," *Astrophys. J. Suppl. Ser.* **191**(2), 376–388 (2010).
10. N. Regnault et al., "The dice calibration project. Design, characterization, and first results," *Astron. Astrophys.* **581**, A45 (2015).
11. T. C. Larason et al., *Spectroradiometric Detector Measurements*, US Department of Commerce, National Institute of Standards and Technology, Washington, DC (1998).
12. LSST Science Collaboration, P. A. Abell et al., "LSST Science Book, Version 2.0," arXiv: 0912.0201 (2009).
13. P. Ingraham et al., "The LSST calibration hardware system design and development," *Proc. SPIE* **9906**, 99060O (2016).
14. M. Coughlin et al., "A collimated beam projector for precise telescope calibration," *Proc. SPIE* **9910**, 99100V (2016).

15. W. P. Mulligan et al., "Manufacture of solar cells with 21% efficiency," in *Proc. 19th EU PVSEC*, vol. 1 (2004).
16. F. Granek, "High-efficiency back-contact back-junction silicon solar cells," The University of Freiburg in Breisgau, Germany (2009).
17. J. Liu et al., "Review of status developments of high-efficiency crystalline silicon solar cells," *J. Phys. D: Appl. Phys.* **51**(12), 123001 (2018).
18. M. Lu et al., "Interdigitated back contact silicon heterojunction solar cell and the effect of front surface passivation," *Appl. Phys. Lett.* **91**(6), 063507 (2007).
19. K. Yoshikawa et al., "Silicon heterojunction solar cell with interdigitated back contacts for a photoconversion efficiency over 26%," *Nat. Energy* **2**, 17032 (2017).
20. C. Reichel et al., "Investigation of electrical shading effects in back-contacted back-junction silicon solar cells using the two-dimensional charge collection probability and the reciprocity theorem," *J. Appl. Phys.* **109**(2), 024507 (2011).
21. D. Chan, J. Phillips, and J. Phang, "A comparative study of extraction methods for solar cell model parameters," *Solid-State Electron.* **29**(3), 329–337 (1986).
22. N. Enebish et al., "Numerical analysis of solar cell current-voltage characteristics," *Solar Energy Mater. Solar Cells* **29**(3), 201–208 (1993).
23. A. Hovinen, "Fitting of the solar cell IV-curve to the two diode model," *Phys. Scr.* **T54**, 175–176 (1994).
24. H. Chu et al., "Soft breakdown behavior of interdigitated-back-contact silicon solar cells," *Energy Procedia* **77**, 29–35 (2015).
25. A. Jain and A. Kapoor, "A new method to determine the diode ideality factor of real solar cell using Lambert w-function," *Solar Energy Mater. Solar Cells* **85**(3), 391–396 (2005).
26. K. Emery et al., "Linearity testing of photovoltaic cells," in *IEEE 4th World Conf. Photovoltaic Energy Conf.*, vol. 2, pp. 2177–2180 (2006).
27. B. H. Hamadani et al., "Non-linearity measurements of solar cells with an led-based combinatorial flux addition method," *Metrologia* **53**(1), 76–85 (2016).
28. A. S. Gudovskikh and J. P. Kleider, "Capacitance spectroscopy of amorphous/crystalline silicon heterojunction solar cells at forward bias and under illumination," *Appl. Phys. Lett.* **90**(3), 034104 (2007).
29. I. Mora-Seró et al., "Recombination rates in heterojunction silicon solar cells analyzed by impedance spectroscopy at forward bias and under illumination," *Solar Energy Mater. Solar Cells* **92**(4), 505–509 (2008).
30. Thorlabs, "Fiber-coupled LEDs," https://www.thorlabs.com/newgrouppage9.cfm?objectgroup_id=5206 (2020).
31. H. Nyquist, "Thermal agitation of electric charge in conductors," *Phys. Rev.* **32**, 110–113 (1928).

Sasha Brownsberger is a graduate student seeking his PhD at Harvard University, working with Professor Christopher Stubbs. He received his BS degree in physics and mathematics from Stanford University in 2010. His current research interests include the search for astronomical probes to study the expansion history of the universe and the development of the next generation of astronomical detectors.

Nicholas Mondrik is a PhD student at Harvard University working with Professor Christopher Stubbs. His current research interests include calibration of large-scale photometric surveys, development of astronomical instrumentation and calibration hardware, and the study of M-dwarfs as exoplanet hosts.

Christopher W. Stubbs is a professor of physics and astronomy at Harvard University. He received his BS degree in physics from the University of Virginia. He received his PhD in physics from the University of Washington.